



ORIGINAL RESEARCH

Design and 3D printing of porous cavity insulation structure for ultra-high electrical withstanding capability

Xiong Yang¹  | Guangyu Sun²  | Baipeng Song¹ | Wenhui Han¹ | Chao Wang¹ |
Wendong Li¹ | Shu Zhang¹ | Falun Song³ | Fangzheng Zou¹ | Guanjun Zhang¹

¹State Key Laboratory of Electrical Insulation and Power Equipment, School of Electrical Engineering, Xi'an Jiaotong University, Xi'an, China

²Ecole Polytechnique Fédérale de Lausanne (EPFL), Swiss Plasma Center (SPC), Lausanne, Switzerland

³Institute of Applied Electronics, China Academy of Engineering Physics, Mianyang, China

Correspondence

Guanjun Zhang and Baipeng Song.
Email: gjzhang@xjtu.edu.cn and
bpsong@mail.xjtu.edu.cn

Associate Editor: Chuanyang Li

Funding information

National Natural Science Foundation of China,
Grant/Award Numbers: 51827809, 52207172,
12175176; China Postdoctoral Science Foundation,
Grant/Award Number: 2021M702564

Abstract

Vacuum-dielectric interface is the most vulnerable part of vacuum insulation systems where surface electrical breakdown is prone to happen, hence severely restricts the development of advanced electro-vacuum devices with large capacity and its miniaturisation. Generally, a direct and effective way to improve vacuum surface insulation is to alleviate the initiation and development of multipactor phenomena. Inspired by this approach, the authors report a 3D-printed insulation structure designed with a millimetre-scale surface cavity covered by periodic through-pore array via stereolithography, exhibiting remarkable multipactor suppression and flashover threshold improvement, well outperforming the conventional flashover mitigation strategies. Experiments and simulations demonstrate that electrons in the multipactor region pass through-pores and are unlikely to escape from the cavity, hence no longer participate in the above-surface multipactor process, and eventually improve flashover threshold. The proposed approach provides new inspiration for the design of advanced insulators featuring ultra-high electrical withstanding capability and brings up new insight into pertinent industrial applications.

1 | INTRODUCTION

Solid insulator is widely adopted in a range of electrical devices using vacuum as the insulating medium or operating in vacuum ambient, including pulsed-power devices, vacuum interrupters, satellites, and many other electrovacuum devices designated to separate conductors and provide mechanical support [1–5]. However, the breakdown will preferentially occurs over the vacuum-dielectric interface (i.e., flashover) under high electric field (E-field) due to the fact that the insulation strength of the vacuum-dielectric interface is much weaker than pure vacuum and bulk insulator, leaving the interface the weakest link in vacuum insulation system [6]. This has become a major concern affecting the reliability, minimisation and operation longevity of above electrical devices, falling significantly short

of the ever-increasing demands for more robust vacuum insulation systems [7]. The occurrence of flashover may incur degraded insulation capability and device performance due to transient electrical and thermal damage. Designing an insulator that would resist flashover while overcoming the limitations of existing flashover mitigation approaches is therefore crucial for the future implementation of high-performance insulators, especially in the rapidly growing field of advanced electrical devices.

Over the past decades, several models have been proposed to expatiate the vacuum flashover phenomenon, among which the secondary electron emission avalanche (SEEA) model is the most widely accepted [8–11]. The flashover process, according to the SEEA theory, is approximately divided into three phases: initiation (i.e., field electron emission from

This is an open access article under the terms of the [Creative Commons Attribution](https://creativecommons.org/licenses/by/4.0/) License, which permits use, distribution and reproduction in any medium, provided the original work is properly cited.

© 2023 The Authors. *High Voltage* published by John Wiley & Sons Ltd on behalf of The Institution of Engineering and Technology and China Electric Power Research Institute.

cathode), development (i.e., multipactor and surface charging), and breakdown (i.e., gas desorption and plasma discharge) [8, 9]. For the cathode-initiated flashover, the seed electrons originate from the field emission from the junction of the cathode, insulator, and vacuum, that is, the cathode triple junction (CTJ), where the E-field strength is significantly higher. An electron accelerated by the external electric field will collide with the dielectric surface and release secondary electrons (SEs), which then form a cascade of SEs, also called as multipactor [12, 13], over the dielectric surface towards the anode. Finally, the Townsend-like plasma discharge breakdown occurs above the insulator surface as local desorbed neutral pressure increases [14]. Therefore, it can be inferred that the most expedient way to mitigate vacuum flashover is to inhibit the development of at least one of the three phases in vacuum flashover process.

Based on the above theories, numerous approaches have been developed to tailor the insulator properties from different perspectives in order to alleviate one of the three phases of flashover, aiming to improve vacuum surface insulation. Suppressing the flashover initiation is supposed to be efficient where techniques including supplement of corona ring [15], insulator geometry optimisation [16], and functionally graded materials (FGM) [17] have been applied to reduce the E-field concentration near the CTJ and to alleviate the field electron emission from the cathode. Particularly, FGM exhibits distinct advantages in suppressing E-field distortion, alleviating the flashover voltage, and simplifying the insulator structure. Despite a variety of innovative attempts, for example, lamination [18], centrifugation [19], electrophoresis [20], magnetophoresis [21], flexible casting [22], and 3D printing [23], a facile yet cost-effective preparation of a high-quality FGM insulator remains a formidable challenge.

Comparatively, multipactor suppression is the more direct, effective, and frequently used strategy, which is based on the design principle to reduce the secondary electron yield (SEY) of the insulators and reduce the number of electrons available for SEEA. The SEY reduction approaches, including bulk insulation modification (e.g., chemical grafting [24, 25], doping of functional fillers [26, 27]) and surface treatment (e.g., fluorination [28, 29], composite coating [30–33], plasma treatment [34–36], and thin film deposition [37, 38]) have shown the ability of multipactor suppression to some extent. Nevertheless, most of these methods are collectively cumbersome and have poor mechanical stability. Alternatively, surface structure alteration techniques show the most promise in adequately suppressing multipactor by physically impeding the movement of electrons over insulator surface. While several surface alterations have been proposed to suppress multipactor such as creating non-periodic roughness [39], pores [40], or grooves [41], the multipactor suppression is still limited owing to the trapped electrons in these structures may escape again and participate in the further SEs growth.

In this work, we start with the previous approaches and report that an insulation structure with a millimetre-scale surface cavity covered by periodic through-pore array exhibits

outstanding multipactor suppression and surface insulation performance in vacuum. The cavity structure is designed to collect electrons passing through these pores. Trapped electrons are unlikely to escape from cavity, and thus no longer participate in the above-surface multipactor process [42]. Meanwhile, the overall mechanical strength of the insulator is fully preserved because the cavity depth is only a few millimetres which is short relative to the typical insulator width. Cavity structures with various structural parameters were fabricated via high-precision 3D printing technology. Subsequently, the effects of the cavity structural parameters on multipactor suppression are systematically investigated by combining experiment and simulation. This work provides a novel and effective strategy to suppress multipactor and potentially inspires further development of flashover mitigation strategies.

2 | EXPERIMENTAL SECTION

2.1 | Design and fabrication of cavity insulation structure

Cavity structures covered by periodic through-pore array were fabricated using a photosensitive resin curing process, namely the laser-based stereolithography apparatus (SLA) technique [43], as illustrated in Figure 1a. As proof of concept, a rectangular mesh with a matrix of square pores is considered in this study. Noted that other geometrical arrangements and pores are also possible. The close-up cross-section diagram and the structural parameters of the cavity structure are shown in Figure 1b, in which the parameter L of the cavity structure represents the gap between the upper and the lower surface, Q is the distance between adjacent pores, and W is the edge length of the square through-pore. The cavity structures of the 3D models used for printing were designed in SolidWorks.

Acrylate resin (High Temp, Formlabs Inc., USA), which is sensitive to UV light radiation of 405 nm was used as the 3D printing resin [44]. The resin was printed using a layer-by-layer process to form the insulator bulks. The layer thickness is set as 50 μm , with an exposure time of 0.8 s under a light intensity of 2.5 mWcm^{-2} to ensure adequate interlayer curing in the printing process. In addition, the lifting speed of the building platform is set to 5 mm/s to stabilise the peeling process from resin tank. Subsequently, the printed parts were washed in ethanol to remove the uncured resin, and then post-cured for 2 h under UV light exposure (75 mWcm^{-2}) at 60 $^{\circ}\text{C}$ to guarantee adequate crosslinking. Finally, the printed parts with a size of 50 \times 50 mm were obtained for testing. In a typical experiment, the thickness of the upper surface (i.e., the through-pores surface) was set to 1 mm throughout this work. The printed parts with various structural parameters were named as $W \times L.yQz$, where x , y , and z represent the value (unit is set to millimetres) of the structural parameters W , L , and Q respectively. Figure 1c compares the representative 3D-printed parts with different structural parameters.

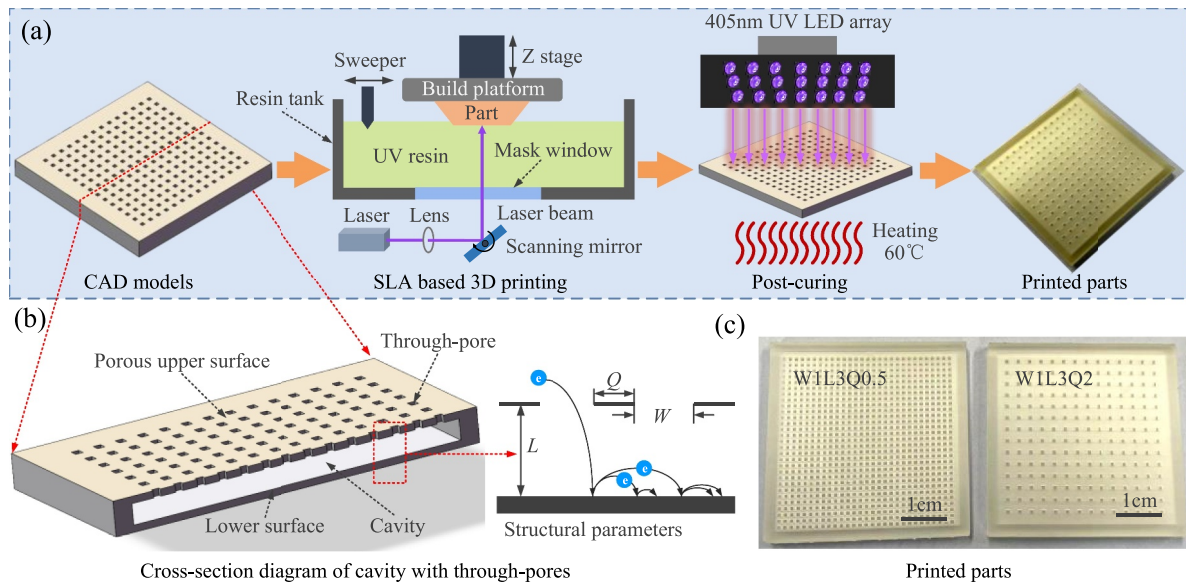


FIGURE 1 Preparation and design of surface cavity insulator with through-pores. (a) Schematic illustration of the 3D printing process, (b) cavity structure with through-pores surface, and (c) representative printed parts with different structural parameter.

2.2 | Characterisation

The cross-sectional morphology of 3D printed parts was carried out by field emission scanning electron microscope (SEM, ZEISS GeminiSEM 500). Additionally, surface optical images of the through-pores were examined using a polarizing microscope (PM, Olympus BX51-P).

Surface insulation strength and potential distribution measurements in vacuum were implemented in a self-designed vacuum chamber with an ambient pressure of 10^{-4} Pa [45]. The electrode-sample configuration used for direct current (DC) and impulse flashover measurements is shown in Figure 2a. Negative standard lightning impulse voltage (1.2/48 μ s) generated by a Marx generator was applied to the tested samples for impulse flashover testing. In this study, the impulse flashover voltages were characterised by a conventional method including three voltage terms (i.e., first breakdown voltage U_{fb} , conditioned voltage U_{co} and hold-off voltage U_{ho}). More details of the evaluation method used for impulse flashover are described in our previous study [31]. In addition, the surface luminescence of the discharge channels after flashover was observed using an intensified charge-coupled device (ICCD, Andor iStar DH334T). A negative DC voltage source with a ramp rate of -500 V/s was applied on the stainless steel electrode until flashover occurred to evaluate the DC flashover characteristics of the specimens. Five flashover voltages were recorded for each testing sample, and at least three samples were used for each type of cavity structure. A two-parameter Weibull statistical method was used to analyse the DC flashover performance.

Surface potential distribution after impulse was performed by a vibrating Kelvin probe (Trek 3455ET) connected to an electrostatic voltmeter (Trek 341B) based on the flashover platform mentioned above. The electrode used for the surface

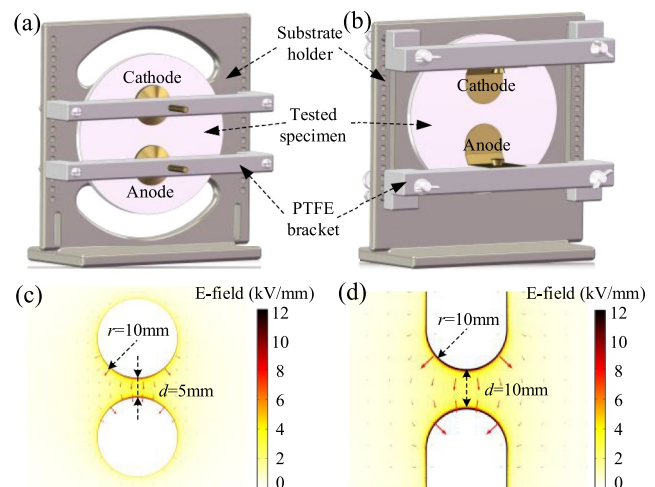


FIGURE 2 Electrode-sample configuration of (a) vacuum flashover and (b) surface potential distribution measurement. Electric field distribution of the electrode-sample configuration for (c) flashover and (d) surface potential distribution measurement.

potential testing is a stainless steel finger-shaped electrode, as illustrated in Figure 2b, which was shaped as semi-circles of 10 mm in radius and 0.7 mm in thickness. The E-field distributions of the electrode-sample configuration used for flashover and surface potential distribution measurements were simulated by COMSOL Multiphysics software, as shown in Figure 2c and d. The E-field distribution of the two electrodes is similar (i.e., strong parallel E-field component), thus it is feasible to analyse the inherent relation of flashover and the surface potential using different electrode structures. The electrode spacing d was adjusted to 10 mm and installed in a 2-axis displacement platform in a sealed chamber to scan the

charging surface of the samples. Kelvin probe is always perpendicular to the sample plane with a ~ 2 mm fixed space between the probe and the sample surface to acquire a high resolution during the whole scanning process. The scanning trajectory of the probe is a zigzag scanning route and covers a region of 40×30 mm at the sample surface after a certain impulse number N . More details of the experiment system and measurement procedures can be found in our previous study [46]. It is worth mentioning that the dissipation of surface charge in vacuum can be neglected during the complete scanning process of 5 min.

3 | RESULTS AND DISCUSSION

3.1 | Printing quality and precision

The choice of appropriate candidate for printed parts of the insulator is primarily determined by their printing quality and precision. Therefore, a first investigation is performed to access a range of structural parameters of the printed parts concerning the printing quality and microstructures. The cross-sectional SEM images of the printing parts in Figure 3a and b show that the matrix of the printing parts is uniform, with no perceptible hole-type defect or crack. The top-view optical micrographs (Figure 3c and d) of the representative porosity surface (i.e., parameter W is 0.5 and 1 mm, respectively) and corresponding square pore size histograms (Figure 3e and f) clearly show that the shape and dimension of the printed through-pores are uniform and the contour is clear. The mean diameters of the printed square pores with parameters W of

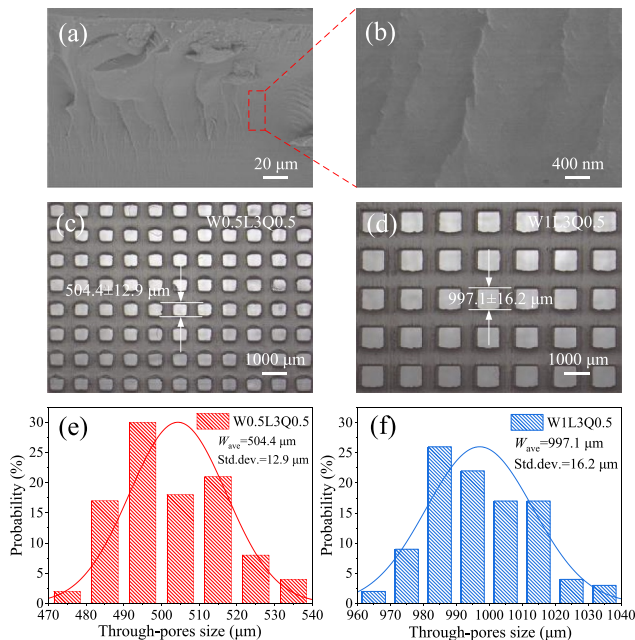


FIGURE 3 Microscopic morphologies of 3D-printed parts. (a) and (b) Cross-sectional SEM image under different scales. Surface optical images of (c) W0.5L3Q0.5 and (d) W1L3Q1. Size histograms of the through-pores of (e) W0.5L3Q0.5 and (f) W1L3Q10.5.

0.5 and 1 mm are 504.4 ± 12.9 μm and 997.1 ± 16.2 μm , respectively. The above observations demonstrate the feasibility of using laser-based SLA technique to fabricate the proposed cavity insulation structures.

3.2 | Experimental verification of multipactor suppression

3.2.1 | Influence of cavity structure on the electric field and flashover channels

To analyse the impact of cavity structures on E-field distribution, the E-field simulations of the flat surface and the cavity structure were conducted. Figure 4 shows the E-field distribution of the flat surface and the cavity structure along the centreline of the sample surface. It was found that the proposed cavity structures do not significantly disturb the E-field at the middle region of the sample so that its effect can be ignored. In contrast, the existence of the cavity structure alleviates the E-field concentration near the CTJ to a certain extent, which is conducive to the suppression of flashover initiation.

The cavity structure with only half surface covered by through-pore array is specially designed to illustrate the effectiveness of the proposed insulation structures design. Flashover channel over the sample surface was observed directly by the ICCD camera, as shown in Figure 5. The insulation structure is fixed by electrodes such that the porous side and non-porous side are symmetrically located across the midplane (Figure 5a). Electrons passing through the pores enter a large vacuum zone and are unlikely to return to the surface, hence mitigating the formation of multipactor due to SE emission avalanche and improving the surface flashover threshold [47, 48].

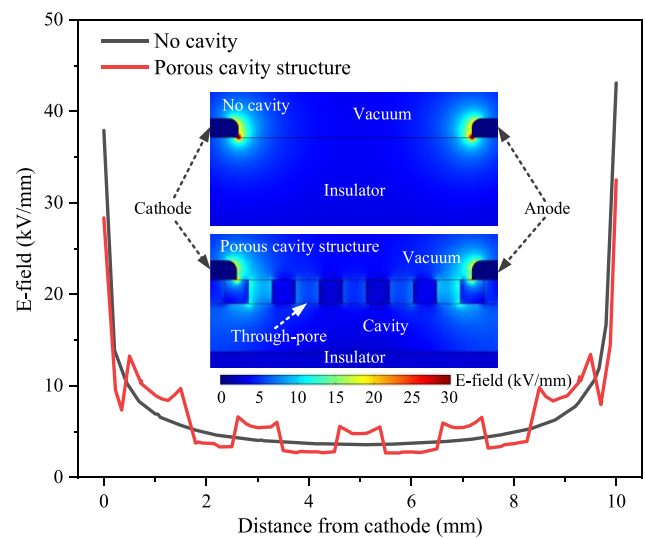


FIGURE 4 Comparison of electric field distribution between the flat surface and cavity structure along the centreline of sample surface.

To verify this, flashover channels were observed 30 times for each sample to investigate the positions of flashover channels and their occurrence probabilities. The observed flashover channels, as expected, always occur on the non-porous side of insulator surface (Figure 5c), indicating higher surface insulation strength on the porous side. Meanwhile, the close-up view of the flashover channels in Figure 5f shows that the flashover channels occur in the interstice between the adjacent through-pores of the upper surface. The flashover discharge intensity (channel width and brightness) of the half-porosity surface is significantly weaker than that of the uniform

porosity surface. This is due mainly to the fact that the surface flashover voltage of the non-porous side (19.87 kV) is significantly lower than that of the uniform porosity surface (32.46 kV). Notably, if flashover channels occur in the lower surface of cavity, the through-pores should exhibit a higher lightness than the other areas of the upper surface. More specifically, the flashover channels occur on the upper surface instead of the lower surface and the through-pores are beneficial to inhibiting the SEEA process, which confirms our hypothesis of multipactor suppression using the proposed insulator design.

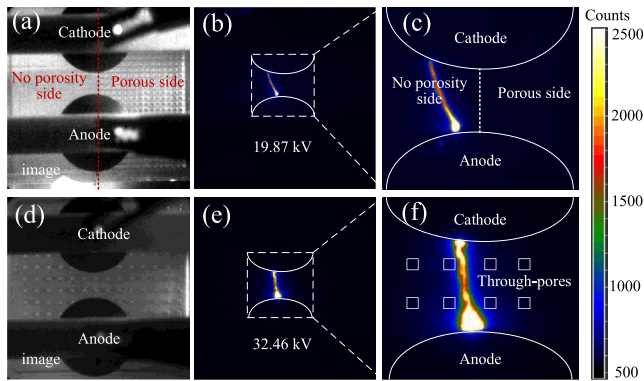


FIGURE 5 Surface flashover channels of the cavity structures. (a) Optical images and (b, c) flashover channels of the half-porosity surface. (d) Optical images and (e, f) flashover channels of the uniform porosity surface.

3.2.2 | Flashover mitigation in vacuum

To quantitatively evaluate the flashover voltage improvement by the through-pores structure, three parameters are chosen to characterise the dimension and distribution of the pores, including the cavity depth L , width W and distance Q between adjacent pores. The parameter L mainly affects electron trajectory in the cavity region and determines the probability that SEs induced by electrons entering the cavity through the through-pores can return to the upper surface. Figure 6a presents the impulse flashover voltage of the insulation structure with various cavity depths and fixed W and Q ($W = 1$ mm, $Q = 0.5$ mm). Clearly, the flashover voltages increase with the cavity depth and saturate at the depth of 2 mm. The trend implies that the electron returning probability drops quickly as L increases, and is approximately zero for a

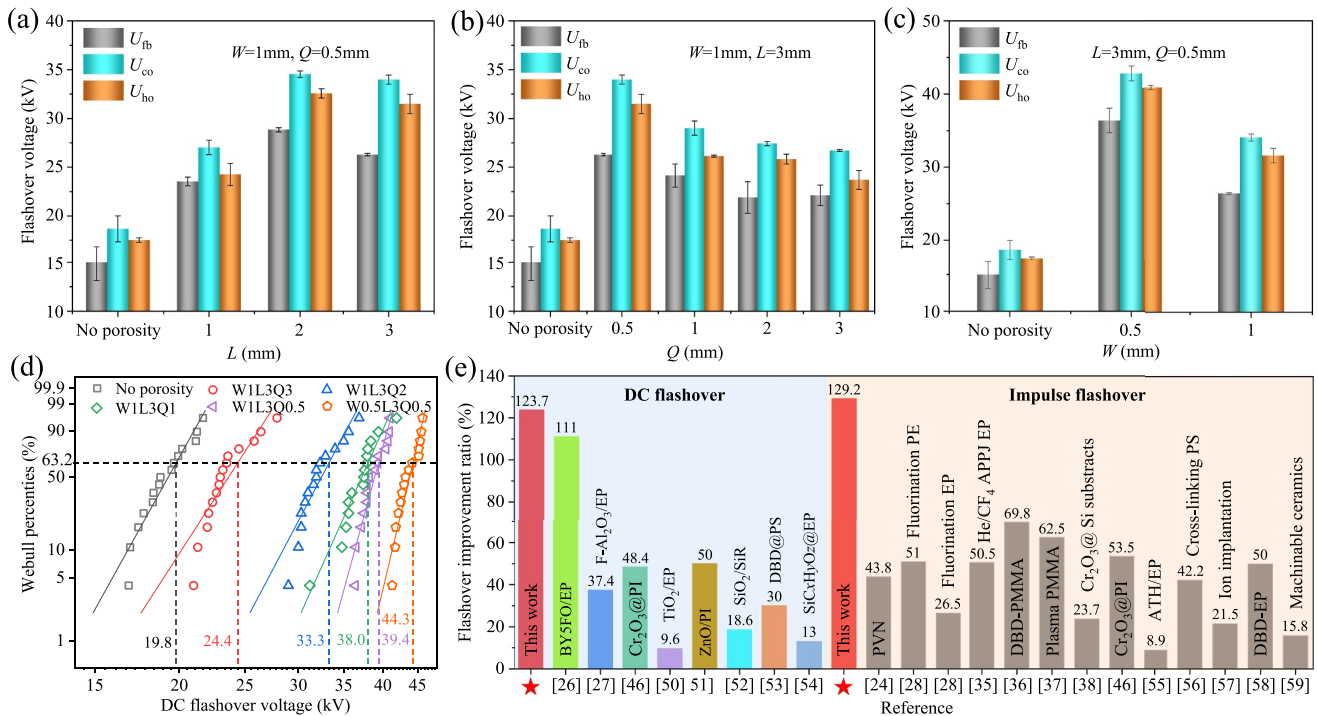


FIGURE 6 Flashover voltage in vacuum of cavity structures. (a-c) Impulse and (d) direct current flashover voltage in vacuum for cavity structures with different structural parameters. (e) Comparison of representative flashover mitigation strategies with this work. EP, PI, PS, PVN, PE, ATH, DBD, and PMMA represent epoxy resin, polyimide, polystyrene, polymerisation of the vinyl naphthalene, polythene, alumina trihydrate, dielectric barrier discharge, and polymethyl methacrylate, respectively.

sufficiently deep cavity. Electrons entering the cavity could further induce secondary electron emission (SEE), if not backscattered, but these SEs will collide more with the side walls of cavity instead of coming back to surface as L increases. Collision with side wall will, however, unlikely to further induce SEE due to low energy of the SEs [8, 9]. The parameter L is hence fixed as 3 mm in the following experiments.

The parameter Q influences the probability of electrons entering the through-pores, in addition to the probability for SEs created at the bottom of cavity to reach the upper surface. The porosity ρ , which is defined as the ratio of removed surface to the total unit cell area in this study, is determined by both the parameters Q and W . Four representative values of pore interval, 0.5, 1, 2, and 3 mm are selected to study its influence, corresponding to porosities 0.44, 0.25, 0.11, and 0.06, respectively. W is fixed as 1 mm and L is 3 mm. Experiment results suggest that flashover voltage increases with porosity, shown in Figure 6b and Table 1. It is worth mentioning that the flashover voltages of the lower porosity level (i.e., W0.5L3Q0.5) are significantly higher than that of the higher (i.e., W1L3Q0.5), as shown in Figure 6c. This could be due to the larger apertures which increase the escape probability for the SEs created at the bottom of cavity to reach the upper. Finally, the highest flashover voltages U_{fb} , U_{co} , and U_{ho} are achieved by the W0.5L3Q0.5, featuring an increase of 142.8% (14.99–36.39 kV), 129.2% (18.68–42.81 kV) and 133.0% (17.53–40.84 kV) relative to the non-porous one, respectively.

The vacuum DC flashover voltage U_f of the insulation structures covered by periodic pore array is analysed to extend its application scenario and is summarised in Figure 6d and Table 1, using a two-parameter Weibull statistics [49].

$$P(U) = 1 - \exp\left[-(U/U_f)^\beta\right] \quad (1)$$

where $P(U)$ is the cumulative probability of surface insulation failure, U is the experimental flashover voltage, Weibull flashover strength U_f is the characteristic flashover strength which refers to a failure probability of 63.2%, and the shape parameter β is associated with the data scattering (the higher the β , the better the reliability). The surface cavity with a periodic through-pore array is shown to improve both U_f and β

of the 3D-printed insulation structures. Meanwhile, the influences of three through-pores parameters on DC flashover voltage are commensurate with the impulsed flashover voltage, and the highest U_f and β are also achieved by the W0.5L3Q0.5 insulators. The flashover voltage is increased from 19.8 to 13.7 kV of the non-porous insulation structures to 44.3 and 32.1 kV of the W0.5L3Q0.5. The DC flashover voltage of W0.5L3Q0.5 is 123.7 % higher than that of the non-porous insulation structures.

To prove the effectiveness of our strategy in improving the vacuum surface insulation, a comparison is carried out between the representative mitigation strategies and our works, as presented in Figure 6e. The aim of the comparison of flashover mitigation strategies is not to achieve quantitative comparison of the flashover voltage increase but to qualitatively analyse the effectiveness of various strategies on the flashover mitigation. It is worth noting that the voltage waveforms and electrode types used in flashover voltage testing in representative literatures selected for comparison are the same or similar to those in this study. Clearly, the cavity insulation structures exhibit ultra-high surface insulation improvement ratio in both the cases of DC [26, 27, 46, 50–54] and impulse [24, 28, 35–38, 46, 55–59] flashover, which far outperform the other flashover mitigation strategies.

3.2.3 | Surface charging behaviours in vacuum

Schottky injection and the SEEA process are known to be the two major causes of surface charging phenomenon in vacuum insulation systems [39]. The SEEA process is much faster than the Schottky injection and subsequent migration process, hence the surface charging is primarily caused by the SEEA, leaving positive surface charges as the SEEA develops [9]. The SEEA process is hard to be captured in real-time by existing diagnostics, so offline measurement of the residual surface charges is frequently chosen as a reference for the development of SEEA, as the number of negative charges in SEEA is equal to the positive charges left on insulator surface. Note that a final breakdown of surface flashover will remove most of the surface charges when a plasma discharge takes place. Therefore, the surface charge measurement is conducted at lower applied voltage to avoid charge dissipation.

To provide more immediate evidence for the SEEA process suppression, the surface charging behaviour (i.e., surface potential distribution) of the representative insulation structures (i.e., non-porous surface, W1L3Q0.5, and W0.5L3Q0.5) after applying -30 kV impulse voltage with various pulse times N were investigated. When an insulation structure is subjected to a high applied voltage, the seed electrons emitted from the CTJ due to field emission are sufficiently accelerated by the parallel field and collide on the surface of the insulator with relatively high energy [47]. The process generates multipactor which propagates towards the anode in the form of SEEA. As shown in Figure 7a–c, the positively charged region expands with repeated pulses and reaches saturation when excitation pulse N is equal to 50, indicating the saturated stage of SEEA.

TABLE 1 Impulse and direct current (DC) flashover voltage of insulation structures with and without through-pores in vacuum.

Specimen	Impulse flashover (kV)			DC flashover (kV)	
	U_{fb}	U_{co}	U_{ho}	U_f	β
No porosity	14.99	18.68	17.53	19.79	13.72
W1L3Q3	22.12	26.71	23.69	24.40	11.80
W1L3Q2	21.89	27.43	25.83	33.30	14.42
W1L3Q1	24.14	29.00	26.12	38.03	17.00
W1L3Q0.5	26.28	33.98	31.48	39.41	27.87
W0.5L3Q0.5	36.40	42.81	40.84	44.30	32.05

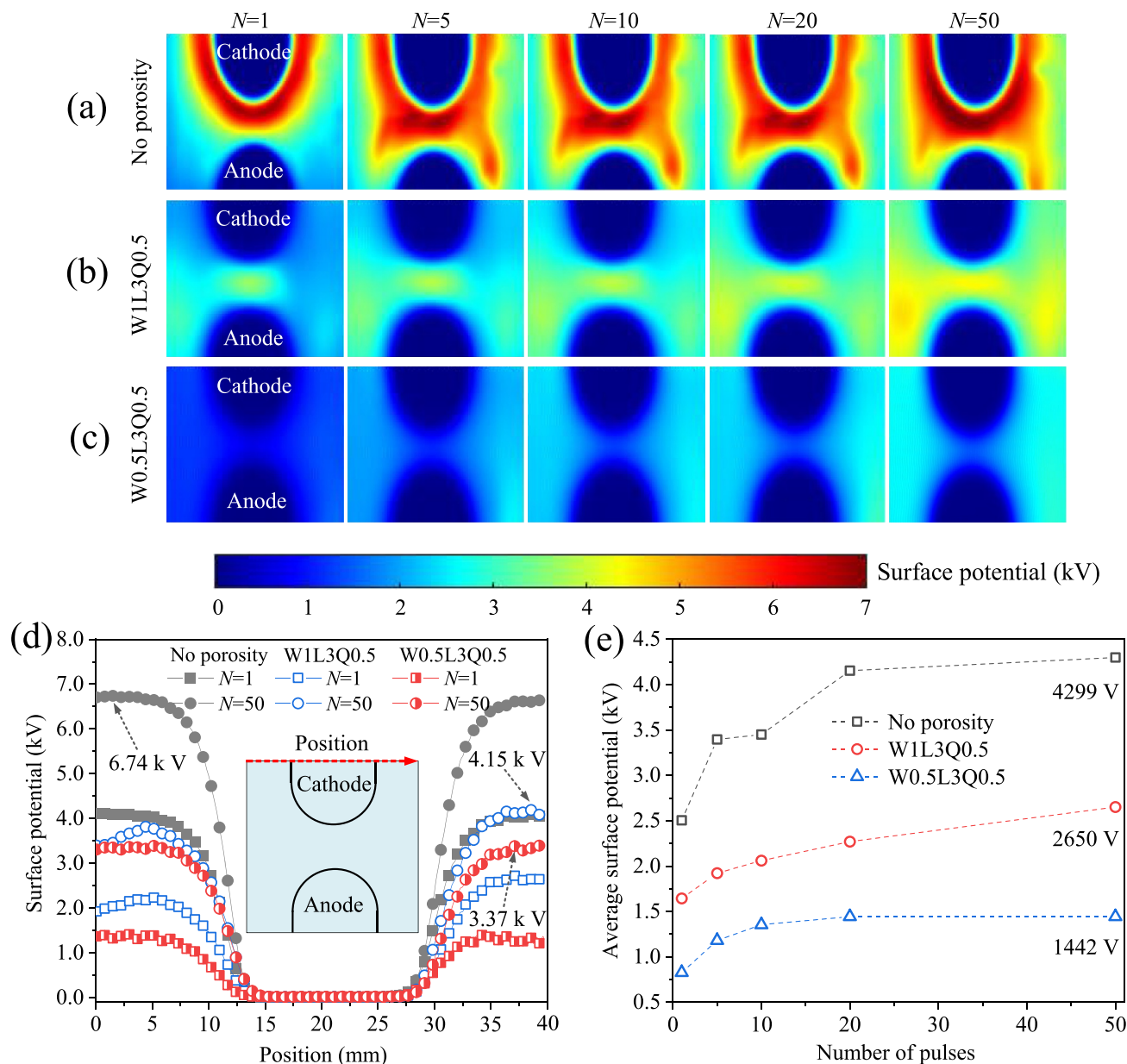


FIGURE 7 Comparison of surface charging behaviours in vacuum between the porous cavity insulation structures and non-porous ones. Surface potential distribution of (a) no porosity, (b) W1L3Q0.5, and (c) W0.5L3Q0.5 after applying -30 kV impulse voltage with different pulses N . (d) Specific potential distribution along a line at $N=1$ and $N=100$, respectively, the inset shows the illustration of the electrode structure and the position of the line. (e) The variations of the average potential with number of pulses.

It is worth mentioning that the positive charges are accumulated at the surface because of abundant electron loss for the material with SEY greater than or equal to 1 during the SEEA process [9, 47]. In general, the saturated surface potential of the non-porous insulation structures is remarkably lower than that of the insulation structures with a porous surface, which implies that the insulation structures with porous surface exhibit excellent multipactor suppression capability.

To quantitatively analyse the multipactor depression effect of the porous cavity structures, the surface potential distribution along the red line nearing the cathode (see the inset of Figure 7d) of the representative insulation structures after multiple pulse

voltage strikes was presented in Figure 7d. The porous surfaces of W1L3Q0.5 and W0.5L3Q0.5 are proven to significantly suppress the surface charge accumulation by reducing the number of SEs in the SEEA process compared to that of a non-porous structure after 50 pulses. The highest surface potential of the non-porous insulators is up to 6.74 kV after reaching saturation, that is, N is equal to 50. In contrast, the highest surface potential of the W1L3Q0.5 and W0.5L3Q0.5 is only 4.15 and 3.37 kV under the same testing conditions, respectively. Furthermore, the average surface potential of the entire sample surface for different numbers of pulses was calculated and shown in Figure 7e. As expected, as the pulse times increase, the

average surface potential gradually increases and reaches saturation when $N = 50$. Meanwhile, the average surface potential of the insulation structures with porous upper surface is clearly lower than the non-porous insulation structures under matching conditions. More precisely, the W0.5L3Q0.5 possesses a better charge suppression capability than the W1L3Q0.5, which is well agreeable with the measurement results of flashover voltage (see Figure 6c).

To further validate the effect of porous cavity structure on the multipactor suppression, the surface potential distribution of half-porosity insulation structures for different numbers of pulses N under -30 kV was measured, as presented in Figure 8a–d. Note that the cavity structural parameters of the porous region, that is, the left side is W1L3Q0.5 and the right

side is a non-porous smooth surface. As expected, fewer charges accumulated on the left half of the insulation structures while the surface charging behaviour remains the same as that of the non-porous surface (see Figure 7a) in the right non-porous region, which is in good agreement with the flashover channels of the half-porosity insulation structures (Figure 5c).

Specific potential variations of the half-porosity insulation structures along the perpendicular bisector (the blue dashed one shown in Figure 8a) of the connection between the cathode and anode with impulse times are shown in Figure 8e. The positively charged region progressively expands on the surface with the increase of impulse times and finally achieves saturation ($N = 50$). In addition, the highest surface potential on the right non-porous region (up to 7.2 kV) is much higher than that on the left porous region (approximated 5.7 kV) for the saturated scenario that N equals 50. The results of the surface charge accumulation again indicate that the cavity with a through-pore array is viable solution for multipactor suppression.

3.3 | Simulation verification of multipactor suppression

Numerical simulation of SE emission avalanche process above dielectric surface is performed using particle-in-cell (PIC) simulation to explain the increase of flashover strength with vacuum cavity structure. The aim of the simulation is not to achieve quantitative consistency with experiment but to reveal microscopically the influence of cavity structure on the evolution of SEEA process.

The simulation considers two parallel electrodes connected by a dielectric plate. Electrons are emitted from CTJ via field emission. The emission current is calculated by Fowler-Nordheim formula [60]. Electrons emitted from the CTJ (left) are accelerated by the parallel field, then collide on dielectric and trigger SE emission. Anode is located on the right. The SEY of material is calculated by Vaughan's empirical formula and depends on the incident energy and direction of the primary electrons [61]. The entrance holes of vacuum cavity are arranged according to hole dimension in experiment but the dimension parallel to both electrode and dielectric is not considered. In practice, the discharge can occur between the entrance holes. In addition, the typical electron trajectory in the vertical direction in SEEA is within several decades μm , while the depth of the vacuum cavity is several mm, hence several orders of magnitude larger. Therefore, electrons entering the pores are assumed to be absorbed by the bottom layer of cavity structure and will not return to the dielectric surface. Above assumptions inevitably exaggerate the effects of cavity structure on SEEA suppression but should resemble the salient features of the SEEA process over the proposed insulator. Detailed choices of simulation parameters are given here: applied parallel field $E_x = 5 \text{ MVm}^{-1}$, gap distance $d = 1 \text{ cm}$, work function to calculate field emission current $\varphi_e = 4.08 \text{ eV}$, time and space resolution $\Delta t = 0.02 \text{ ps}$, and $\Delta x = 2 \mu\text{m}$. The simulation usually acquires 2×10^5 time steps

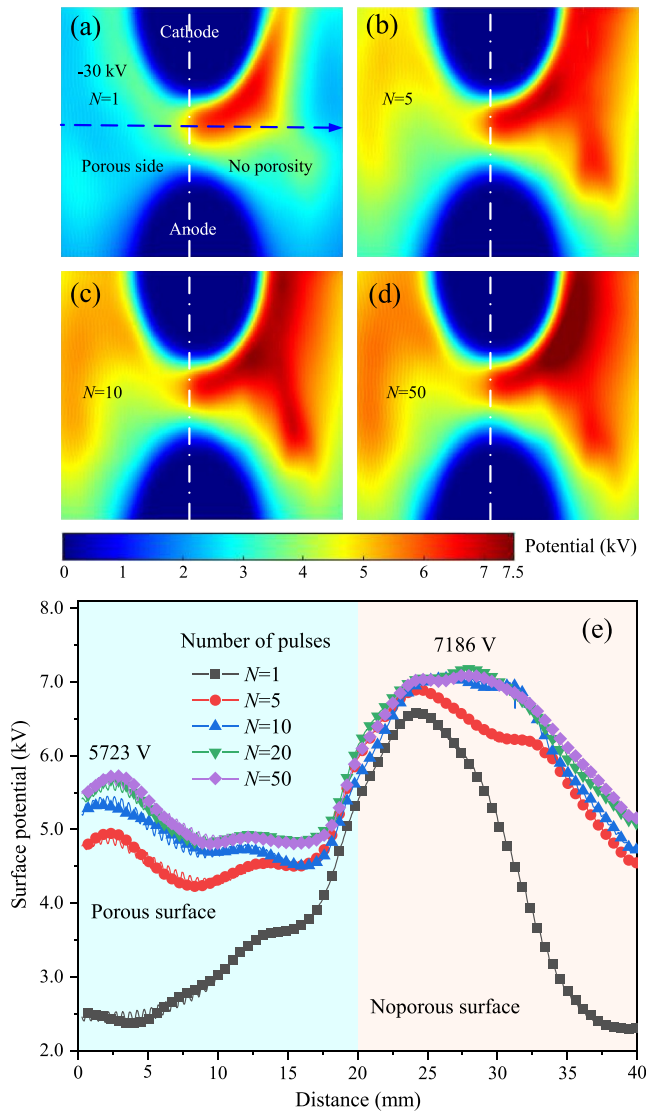


FIGURE 8 Surface potential variations of the half-porosity insulation structures under -30 kV with different pulses N . (a) $N = 1$; (b) $N = 5$; (c) $N = 10$; (d) $N = 50$. (e) Specific potential distribution along the perpendicular bisector of the connection between the cathode and anode electrodes for different numbers of pulses, the blue dashed line in Figure 7a shows the position of the perpendicular bisector.

to converge. Two characteristic parameters in Vaughan's empirical formula are $\delta = 3.0$ and $A_{m0} = 300$ eV, representing the maxima of SEY curve and the related primary electron energy.

The obtained electron distributions after achieving convergence with the same entrance pore width and a series of intervals between holes are shown in Figure 9. With denser entrance hole distribution, the SEEA process is remarkably mitigated. With $Q = 2\text{--}3$ mm, SEEA can still develop between the last entrance on the right and the anode. When $Q = 0.5$ mm, the SEEA is almost entirely suppressed. The mean surface charge density behaviours in accordance with the SEEA process, as the SEEA theory predicts that the negative charges of electrons in SEEA are equal to the accumulated positive surface charges on dielectric [6].

A scan of entrance hole diameter is also performed, shown in Figure 10. The influence of entrance diameter is directly linked with the electron distance of flight in the saturated SEEA regime. A rough estimation of the distance that a newly emitted SE travels between the emission point and the incident point on dielectric, is expressed in the equation below:

$$d_{\text{leap}} = \frac{A_1 - A_0}{E_x e} \quad (2)$$

Here A_1 is the energy required to produce one SE, varying from decades to a hundred eV, A_0 is the initial energy of a SE, typically below 5 eV. e is the elementary charge and E_x is the

parallel electric field. Typical value of d_{leap} is therefore decades μm . Entrance hole diameter comparable with d_{leap} should have limited influence in blocking the development of SEEA. In practice, the pore diameter should be much larger than d_{leap} as electron energy is higher in the initial stage of SEEA. Simulation results in Figure 10 are consistent with above descriptions. Entrance pore with $W = 50, 200$ μm has limited influence and the SEEA continues to develop after passing the pore. When $W = 400$ μm the SEEA develops roughly 4 mm after passing the pore, whereas almost no electron can pass the pore if $W = 800$ μm . In reality, the SEEA can develop over the insulator surface where no through-pores are present even if the pore diameter is sufficiently large, hence the SEEA cannot be fully suppressed.

4 | CONCLUSION

In summary, we fabricated an insulation structure with a millimetre-scale surface cavity covered by periodic through-pore array, which features remarkable multipactor suppression and vacuum surface insulation performance. The porous cavity insulation structures with a range of structural parameters were designed and fabricated via SLA technology. Both experiments and simulations support the effectiveness of the proposed insulation design, and the influences of the cavity structural parameters on multipactor suppression are systematically investigated. It is shown that the designed cavity insulation

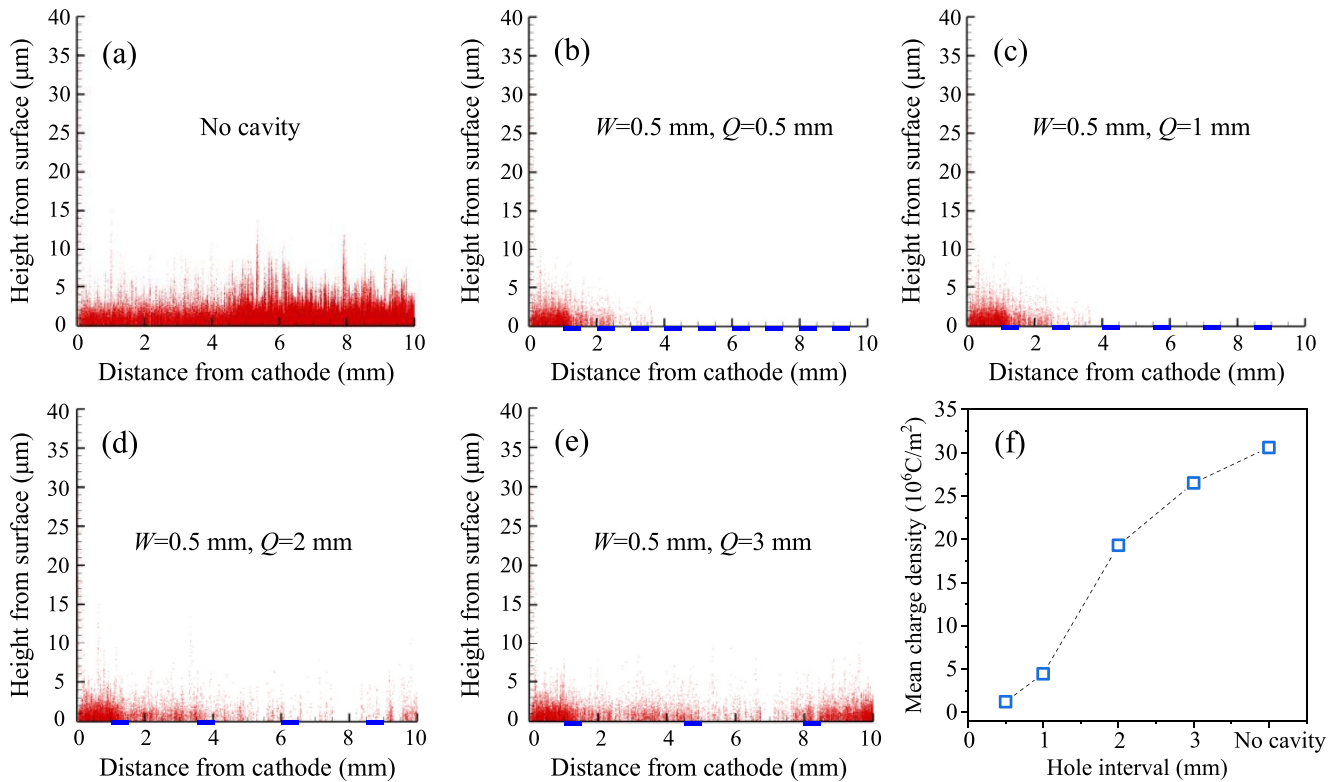


FIGURE 9 Electron distribution over dielectric surface with different values of hole interval. (a) no cavity; (b) $Q = 0.5$ mm; (c) $Q = 1$ mm; (d) $Q = 2$ mm; (e) $Q = 3$ mm. (f) Average surface charge density of (a)–(e). The pore positions are marked out with blue bars.

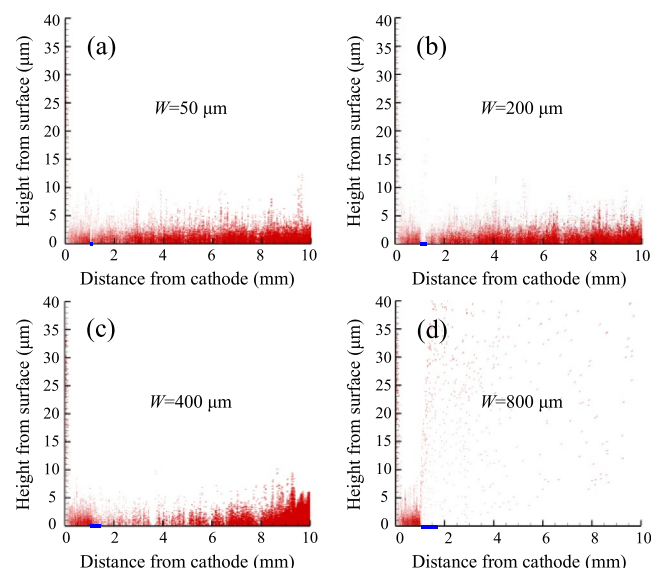


FIGURE 10 Electron distribution over dielectric surface with different diameters of holes. (a) $W = 50 \mu\text{m}$; (b) $W = 200 \mu\text{m}$; (c) $W = 400 \mu\text{m}$; (d) $W = 800 \mu\text{m}$. Only one hole is considered in the four simulation cases. The hole positions are marked out with blue bars.

structures, specifically for the higher porosity one, exhibit excellent multipactor suppression capability and ultra-high surface insulation improvement ratio (129.2% impulse and 123.7% DC vacuum flashover voltage increase, respectively). This work provided a promising approach for designing and fabricating an insulator with high surface insulation in vacuum insulation systems.

ACKNOWLEDGEMENTS

This work was supported by the National Natural Science Foundation of China (Grant No. 51827809, 52207172, 12175176) and the China Postdoctoral Science Foundation (2021M702564).

CONFLICT OF INTEREST

The authors declare no potential conflict of interests.

DATA AVAILABILITY STATEMENT

The data that support the findings of this study are available from the corresponding author upon reasonable request.

ORCID

Xiong Yang  <https://orcid.org/0000-0002-8275-3182>

Guangyu Sun  <https://orcid.org/0000-0001-6761-6019>

REFERENCES

- Zhang, G.J., et al.: Pulsed flashover across a solid dielectric in vacuum. *IEEE Trans. Dielectr. Electr. Insul.* 25(6), 2321–2339 (2018)
- Harris, J.R., et al.: Displacement current and surface flashover. *Appl. Phys. Lett.* 91(12), 121504 (2007)
- Neuber, A.A., et al.: Interface breakdown during high-power microwave transmission. *IEEE Trans. Magn.* 43(1), 496–500 (2007)
- Zhu, M., et al.: Review of interface tailoring techniques and applications to improve insulation performance. *High Volt.* 7(1), 12–31 (2022)
- Zhang, B., et al.: Review of surface transient charge measurement on solid insulating materials via the Pockels technique. *High Volt.* 26(4), 608–624 (2021)
- Sun, G.Y., et al.: Flashover strength improvement and multipactor suppression in vacuum using surface charge pre-conditioning on insulator. *J. Appl. Phys.* 124(13), 134102 (2018)
- Li, S.T.: Improvement of surface flashover in vacuum. *High Volt.* 5(2), 122–133 (2020)
- Anderson, R.A., Brainard, J.P.: Mechanism of pulsed surface flashover involving electron-stimulated desorption. *J. Appl. Phys.* 51(3), 1414–1421 (1980)
- Sun, G.Y., et al.: Estimation of surface flashover threshold in a vacuum II: flashover phase transition. *J. Phys. D Appl. Phys.* 53(7), 075201 (2020)
- Blaise, G., Legressus, C.: Charging and flashover induced by surface polarization relaxation process. *J. Appl. Phys.* 69(9), 6334–6339 (1991)
- Li, C.Y., et al.: The potentially neglected culprit of DC surface flashover: electron migration under temperature gradients. *Sci. Rep.* 7(1), 3271 (2017)
- Wang, H.H., et al.: Effects of rf magnetic field on upstream dielectric multipactor. *Plasma Sources Sci. Technol.* 27(12), 125006 (2018)
- Wright, D., et al.: Multipactor suppression via asymmetric grooves in S-band waveguide. *Phys. Plasmas* 29(6), 063108 (2022)
- Neuber, A., et al.: Electric current in dc surface flashover in vacuum. *J. Appl. Phys.* 85(6), 3084–3091 (1999)
- Ilhan, S., Ozdemir, A.: 380 kV corona ring optimization for ac voltages. *IEEE Trans. Dielectr. Electr. Insul.* 18(2), 408–417 (2011)
- Wang, C., et al.: Dielectrically graded spacer for 126 kV GIS: design and construction strategy. *IEEE Trans. Dielectr. Electr. Insul.* 29(4), 1590–1598 (2022)
- Li, J., et al.: Promising functional graded materials for compact gaseous insulated switchgears/pipelines. *High Volt.* 5(3), 231–240 (2020)
- Zhu, J., et al.: Vacuum surface flashover of high gradient insulators under nanosecond pulse. *IEEE Trans. Plasma Sci.* 42(2), 330–335 (2014)
- Hayakawa, N., et al.: Fabrication and simulation of permittivity graded materials for electric field grading of gas insulated power apparatus. *IEEE Trans. Dielectr. Electr. Insul.* 23(1), 547–554 (2016)
- Shen, Z., et al.: In situ electric field driven assembly to construct adaptive graded permittivity BaTiO₃/epoxy resin composites for improved insulation performance. *Appl. Mater. Today* 20, 100647 (2020)
- Nardi, T., et al.: Graded-permittivity polymer nanocomposites as superior dielectrics. *Compos. Sci. Technol.* 129, 1–9 (2016)
- Hayakawa, N., et al.: Simulation on discharge inception voltage improvement of GIS spacer with permittivity graded materials (epsilon-FGM) using flexible mixture casting method. *IEEE Trans. Dielectr. Electr. Insul.* 25(4), 1318–1323 (2018)
- Li, X.R., et al.: 3D Printing fabrication of conductivity non-uniform insulator for surface flashover mitigation. *IEEE Trans. Dielectr. Electr. Insul.* 26(4), 1172–1180 (2019)
- Mao, J., et al.: Excellent vacuum pulsed flashover characteristics achieved in dielectric insulators functionalized by electronegative halogen-phenyl and naphthyl groups. *Langmuir* 38(13), 4129–4137 (2022)
- Yang, K.R., et al.: Enhancing dielectric strength of epoxy polymers by constructing interface charge traps. *ACS Appl. Mater. Interfaces* 13(22), 25850–25857 (2021)
- Yin, K., et al.: Causation of ultra-high surface insulation of Bi_{0.95}Y_{0.05}-FeO₃/epoxy composites: simultaneous sine-variations of dielectric and trap properties with filler content. *Compos. Sci. Technol.* 197, 108199 (2020)
- Lu, F.C., et al.: Enhanced surface insulation and depressed dielectric constant for Al₂O₃/epoxy composites through plasma fluorination of filler. *J. Phys. D Appl. Phys.* 52(15), 155201 (2019)
- Zhou, R.D., et al.: Mechanism of F₂/N₂ fluorination mitigating vacuum flashover of polymers. *J. Phys. D Appl. Phys.* 52(37), 375304 (2019)
- Chen, S., et al.: Mechanism on improved surface flashover performances in vacuum of epoxy resin using fluorocarbon plasma treatment. *High Volt.* 7(3), 420–428 (2022)
- Zhu, M.X., et al.: Superhydrophobic and high-flashover-strength coating for HVDC insulating system. *Chem. Eng. J.* 404, 126476 (2021)

31. Wang, C., et al.: UV-cured nanocomposite coating for surface charging mitigation and breakdown strength enhancement: exploring the combination of surface topographical structure and perfluorooctyl chain. *RSC Adv.* 10(28), 16422–16430 (2020)
32. Wang, C., et al.: Study on the vacuum flashover of insulator with fluorosilane modified nanocomposite UV curable coating. *High Volt. Eng.* 43(1), 1–4 (2017). (in Chinese)
33. Xie, Q., et al.: The synergistic effect of micro structure/nanofiller/superhydrophobicity on the surface flashover. *High Volt.* 7(6), 1091–1098 (2022)
34. Kong, F., et al.: Two-phase-interfaced, graded-permittivity titania electrical insulation by atmospheric pressure plasmas. *ACS Appl. Mater. Interfaces* 14(1), 1900–1909 (2022)
35. Chen, S., et al.: Surface modification of epoxy resin using He/CF₄ atmospheric pressure plasma jet for flashover withstanding characteristics improvement in vacuum. *Appl. Surf. Sci.* 414, 107–113 (2017)
36. Shao, T., et al.: Surface modification of polymethyl-methacrylate using atmospheric pressure argon plasma jets to improve surface flashover performance in vacuum. *IEEE Trans. Dielectr. Electr. Insul.* 22(3), 1747–1754 (2015)
37. Shao, T., et al.: Enhanced surface flashover strength in vacuum of polymethylmethacrylate by surface modification using atmospheric-pressure dielectric barrier discharge. *Appl. Phys. Lett.* 105(7), 071607 (2014)
38. Zhu, M.D., et al.: Microstructures and electrical properties of nano-structured Cr₂O₃ thin films deposited by dual-target reactive high-power impulse magnetron sputtering. *Vacuum* 164, 293–299 (2019)
39. Guo, B.H., et al.: Mechanism of vacuum flashover on surface roughness. *J. Phys. D Appl. Phys.* 52(21), 215301 (2019)
40. Ye, M., Wang, D., He, Y.: Mechanism of total electron emission yield reduction using a micro-porous surface. *J. Appl. Phys.* 121(12), 124901 (2017)
41. Huo, Y., et al.: Sharp improvement of flashover strength from composite micro-textured surfaces. *J. Appl. Phys.* 122(11), 115105 (2017)
42. Weber, E.D., et al.: Experimental verification of multipactor suppression in microstripline using high porosity surfaces. *IEEE Trans. Plasma Sci.* 50(1), 43–49 (2022)
43. Domingo-Roca, R., Jackson, J.C., Windmill, J.F.C.: 3D-printing polymer-based permanent magnets. *Mater. Des.* 153, 120–128 (2018)
44. Li, W.D., et al.: Stereolithography based additive manufacturing of high-k polymer matrix composites facilitated by thermal plasma processed barium titanate microspheres. *Mater. Des.* 192, 108733 (2020)
45. Wang, C., et al.: Unraveling the role of surface molecular structure on vacuum flashover for fluorinated copolymers. *Appl. Surf. Sci.* 505, 144432 (2020)
46. Yang, X., et al.: Ultralow secondary electron emission and improved vacuum surface insulation of polyimide with scalable nanocomposite coating. *Appl. Surf. Sci.* 592, 153221 (2022)
47. Zhang, S., et al.: Modelling vacuum flashover mitigation with complex surface microstructure: mechanism and application. *High Volt.* 5(2), 110–121 (2020)
48. Zhang, J.W., et al.: Evolution of vacuum surface flashover for angled dielectric insulators with particle-in-cell simulation. *Phys. Plasmas* 29(4), 043506 (2022)
49. Ren, L., et al.: High-temperature high-energy-density dielectric polymer nanocomposites utilizing inorganic core-shell nanostructured nanofillers. *Adv. Energy Mater.* 11(28), 2101297 (2021)
50. Li, S., et al.: DC surface flashover of epoxy nanocomposites in vacuum using rare methodologies to achieve unique results. *IEEE Nanotechnol. Mag.* 12(2), 6–14 (2018)
51. Zhang, Z.J., et al.: Surface flashover characteristics in polyimide/ZnO nanocomposite under dc voltage in vacuum. *IEEE Trans. Dielectr. Electr. Insul.* 22(5), 2951–2957 (2015)
52. Liu, Y., Li, Z.L., Du, B.X.: Effects of nano-SiO₂ particles on surface tracking characteristics of silicone rubber composites. *Appl. Phys. Lett.* 105(10), 102905 (2014)
53. Kong, F., et al.: Surface modifications of polystyrene and their stability: a comparison of DBD plasma deposition and direct fluorination. *Appl. Surf. Sci.* 459, 300–308 (2018)
54. Xie, Q., et al.: Deposition of Si_xH_yO_z thin film on epoxy resin by nanosecond pulsed APPJ for improving the surface insulating performance. *Plasma Sci. Technol.* 20(2), 025504 (2018)
55. Zhao, W.B., et al.: Correlation between trapping parameters and surface insulation strength of solid dielectric under pulse voltage in vacuum. *IEEE Trans. Dielectr. Electr. Insul.* 14(1), 170–178 (2007)
56. Mao, J., et al.: Enhancing the surface flashover strength of polystyrene in vacuum by secondary electron emission suppression through cross-linking. *Langmuir* 37(13), 3903–3911 (2021)
57. Zhu, M., et al.: Surface insulating properties of titanium implanted alumina ceramics by plasma immersion ion implantation. *Nucl. Instrum. Methods Phys. Res. B.* 407, 155–159 (2017)
58. Chen, X.Y., et al.: Promotion of epoxy resin surface electrical insulation performance and its stability by atmospheric fluorocarbon dielectric barrier discharge. *IEEE Trans. Dielectr. Electr. Insul.* 27(6), 1973–1981 (2020)
59. Zheng, N., et al.: Influence of surface carburization of machinable ceramics on its pulsed flashover characteristics in vacuum. *Plasma Sci. Technol.* 13(6), 656–660 (2011)
60. Fowler, R.H., Nordheim, L.: Electron emission in intense electric fields. *Proc. R. Soc. Lond. - Ser. A Contain. Pap. a Math. Phys. Character* 119(781), 173–181 (1928)
61. Vaughan, R.M.: Secondary emission formulas. *IEEE[36. Trans. Electron. Devices.* 40(4), 830 (1993)

How to cite this article: Yang, X., et al.: Design and 3D printing of porous cavity insulation structure for ultra-high electrical withstanding capability. *High Voltage.* 1–11 (2023). <https://doi.org/10.1049/hve2.12326>